DOI: 10.11973/jxgccl250378

水工闸门增材修复耐磨焊条堆焊层的组织及性能

朱思思[1,2],胡 兴[1,2],吴溢凡[3],赵建华[2],杨 可[2]
(1. 中国长江电力股份有限公司,武汉 210023; 2. 水资源高效利用与工程安全国家工程研究中心,南京 211100; 3. 河海大学机电工程学院,常州 213000)

摘 要: 设计了一种耐磨焊条,焊条药皮由还原铁粉、海泡石矿、钾长石、水玻璃、金红石、萤石、锰粉、纤维素、铝硅合金、硅铁合金及稀土硅铁组成,焊芯为 0Cr13 不锈钢丝,采用手工电弧焊对 Q235 钢进行水下三层多道堆焊试验,通过与普通焊条堆焊层对比,研究了耐磨焊条堆焊层的组织与耐磨性能。结果表明:耐磨焊条堆焊层中无裂纹等缺陷,其组织为板条马氏体和少量 δ-铁素体,马氏体沿温度梯度方向生长形成柱状晶。与普通焊条相比,耐磨焊条堆焊层的马氏体晶粒尺寸更小、体积分数更高,δ-铁素体含量更少,显微硬度提高,摩擦因数和磨损率降低,耐磨性能更好。耐磨焊条堆焊层的磨损表面存在浅且粗细均匀的犁沟,局部伴有少量剥落、磨屑及微裂纹,主要磨损机制为轻度磨粒磨损。

关键词: 水下焊接; 显微组织; 显微硬度; 耐磨性能
中图分类号: TG401 **文献标志码**: A **文章编号**: 1000-3738(2025)11-0106-07

0 引 言

在长期运行过程中,水工闸门表面受到含砂水流持续冲刷与磨蚀,会产生不同程度的损伤[1-3]。这些损伤不仅会降低设备运行效率,还可能引发结构失效,影响机组的安全稳定运行[4]。传统更换部件的方式存在成本高、施工周期长等不足;水下湿法焊接(UWW)增材修复技术可直接在水中对水利设施关键设备的损伤部件进行紧急修复,可有效缩短停机时间并降低维护成本[5-8]。然而,受水下低温、高压、高导热性及水体杂质等环境因素制约,UWW 冷却速率过快,气体保护效果不佳,熔池稳定性不足,形成的修复层中产生裂纹、气孔等缺陷,严重影响其服役性能[9-10]。

目前,研究人员主要通过调整焊条药皮成分来改善水下增材修复层的质量[11-12]。研究[12-13]发现:在药皮中引入金红石可以降低扩散氢含量,减少微裂纹与孔隙,从而提高增材修复层的致密程度与可靠性;在药皮中引入适量镍进行合金化,可促使大量针状铁素体(AF)形成,同步提高修复层的塑性与韧性[13]。焊接工艺参数显著影响着修复层的成形质量。研究表明,热输入过低或过高均不利于焊接成形质量:热输入过低易导致未焊透及成形缺陷[14];热输入过高则会引起电弧稳定性下降、金属传输恶化及组织粗化加剧[15]。在多数湿法手工电弧焊工艺中,热输入控制在 1～2 kJ·mm^{-1} 范围内较为适宜[16-18]。

磨损是水工闸门的主要失效形式之一,对其进行修复时,所用材料的耐磨性能与强韧性同等重要。然而,现有 UWW 增材修复研究多聚焦于修复层成形质量、抗裂性及强韧性方面,对于耐磨性能及耐磨机理的研究较少。作者以还原铁粉、海泡石矿、钾长石、水玻璃、金红石、萤石、锰粉、纤维素、铝硅合金、硅铁合金及稀土硅铁为主要药皮组分,配以 0Cr13 马氏体不锈钢焊芯,研制了适用于水工闸门水下修复的耐磨焊条;采用水下湿法手工电弧焊在 Q235 钢基体上进行三层多道堆焊,研究了耐磨焊条增材修复堆焊层的组织与耐磨性能,拟为水工闸门的高耐磨水下增材修复提供材料设计与工艺优化的理论依据。

1 试样制备与试验方法

母材为 Q235 钢,尺寸为 25 mm×40 mm×10 mm。焊接材料为市售普通水下焊条和自研耐磨焊条,市售普通水下焊条具有良好耐腐蚀性能和抗裂性。自研耐磨焊条的焊芯选用 0Cr13 不锈钢丝,尺寸为

收稿日期: 2025-08-15; **修订日期**: 2025-10-09
基金项目: 水资源高效利用与工程安全国家工程研究中心开放研究基金资助项目(GJGCZX-JJ-202408)
作者简介: 朱思思(1988—),男,湖北武汉人,高级工程师,硕士

ϕ3.2 mm×360 mm，0Cr13 不锈钢具有较高的碳和铬含量，因此兼具良好淬硬性、耐磨性能和一定耐腐蚀性能。母材、自研耐磨焊条焊芯和市售普通水下焊条的化学成分见表 1。自研耐磨焊条的药皮组成见表 2，其中金红石、萤石、钾长石与还原铁粉为主要造渣剂和稳弧剂，海泡石矿与纤维素有利于焊接工艺性、药皮结合性[19]及成分均匀性，锰粉、铝硅合金与硅铁合金用于脱氧和合金强化[20]，稀土硅铁则用于细化晶粒、净化夹杂并抑制缺陷生成。按表 2 配料，混合均匀后加入适量模数为 3.3 的钠水玻璃黏结剂，持续搅拌至浆料状态均一，采用手工涂覆方式将药皮浆料均匀按压在焊芯表面，控制药皮厚度为 1 mm，采用 ZY-60 型自控远红外电焊条烘干机进行烘干处理，工艺流程如下：50 ℃ 保温 15 min→100 ℃ 保温 15 min→150 ℃ 保温 60 min，总烘干时间为 90 min。

表 1　Q235 钢、0Cr13 不锈钢丝及普通焊条的化学成分

Table 1　Chemical composition of Q235 steel, 0Cr13 stainless steel wire and common electrode

材料	质量分数/%					
	C	Si	Mn	S	P	Cr
Q235钢	0.14～0.22	≤0.30	0.30～0.65	≤0.050	≤0.045	
0Cr13不锈钢丝	≤0.08	≤1.00	≤1.00	≤0.03	≤0.035	11.50～13.00
普通水下焊条	0.14	≤0.49	0.33～0.78	≤0.038	≤0.06	

表 2　自研耐磨焊条中的药皮配方

Table 2　Chemical composition of flux coating in self-developed wear-resistant electrode

成分	还原铁粉	海泡石矿	钾长石	水玻璃	金红石	萤石	锰粉	纤维素	铝硅合金	硅铁合金	稀土硅铁
质量分数/%	8.33	2.5	4.17	25.83	37.5	8.33	2.5	4.17	2.5	1.67	2.5

采用图 1 所示的水下焊接试验系统，搭配 YK-305AA 型焊机在水深 500 mm 处对母材进行三层多道手工电弧堆焊试验，水箱尺寸为 800 mm×400 mm×600 mm，焊接电流为 140 A，焊接电压为 32 V，焊接速度为 2 mm·s^{-1}[21]。

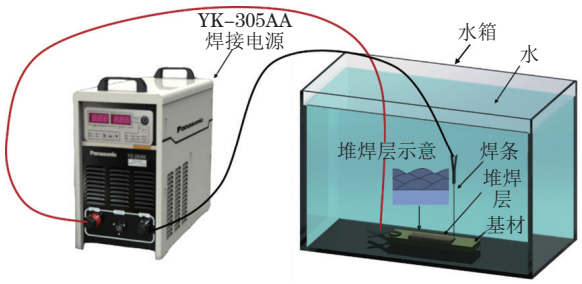

图 1　水下焊接试验系统示意

Fig. 1　Schematic of underwater surfacing welding test system

在堆焊层上切取金相试样，尺寸为 10 mm×10 mm×5 mm，采用 80#～2000# SiC 砂纸依次打磨，用粒径 0.5 μm 金刚石膏抛光，用由 25 g $FeCl_3$+25 mL HCl+100 mL H_2O 组成的混合溶液腐蚀 10 s 后，采用配备 VHX-700F 型超景深显微镜的光学显微镜（OM）观察显微组织。采用 HYHVS-1000AT 型显微维氏硬度计测试横截面显微硬度，载荷为 5 N，保载时间为 20 s，从堆焊层顶端向母材方向每隔 0.2 mm 取点进行测试，相同距离处测 3 个点取平均值。采用 CFT-Ⅰ型材料表面性能综合测试仪进行室温（25 ℃）摩擦磨损试验，对偶件为直径 6 mm 的 Si_3N_4 磨球，施加的载荷为 5 N，往复频率为 3.33 Hz，滑动距离为 4 mm，试验时间为 30 min。采用 VHX-700F 型超景深显微镜观察磨损三维形貌，计算磨损率，计算公式如下：

$$W = V/(LH) = SD/(LH) \quad (1)$$

式中：W 为磨损率；L 为施加载荷；H 为滑动总距离；V 为磨损体积；S 为磨损横截面面积；D 为往复滑动距离。

采用 TESCEN-VEGA4 型扫描电子显微镜（SEM）观察磨损形貌。

2　试验结果与讨论

2.1　显微组织

由图 2 可见，耐磨焊条堆焊层中未见明显裂纹缺陷，组织均为板条马氏体和少量弥散分布的短条状 δ-铁素体。第三层堆焊层因冷却速率较快，马氏体板条排列规整，沿最大温度梯度方向生长形成柱状晶，板条宽度较小，包块尺寸细小，δ-铁素体多呈细条状或点状弥散分布于柱状晶轴附近；第二层堆焊层受第三层焊接热输入影响，会发生局部奥氏体化，

在随后的快速冷却过程中在原有板条界面与位错富集区形成新生细小马氏体[22]，因此这层中的板条马氏体数量相较于第三层堆焊层增多，同时晶粒得到细化，最终这层组织主要为细小板条马氏体，并伴有少量较粗大的板条马氏体；第一层堆焊层经历两次焊接热循环，在第二层热循环作用下组织奥氏体化后淬火形成全马氏体，后续热循环使部分区域回火并析出碳化物，碳的贫化降低了局部奥氏体稳定性，促使板条界处再次发生奥氏体化，在冷却过程中转变为二次细小马氏体，同时未发生奥氏体化的马氏体析出碳原子并转变为少量 δ-铁素体，因此整体仍保持马氏体板条状形貌[23]。

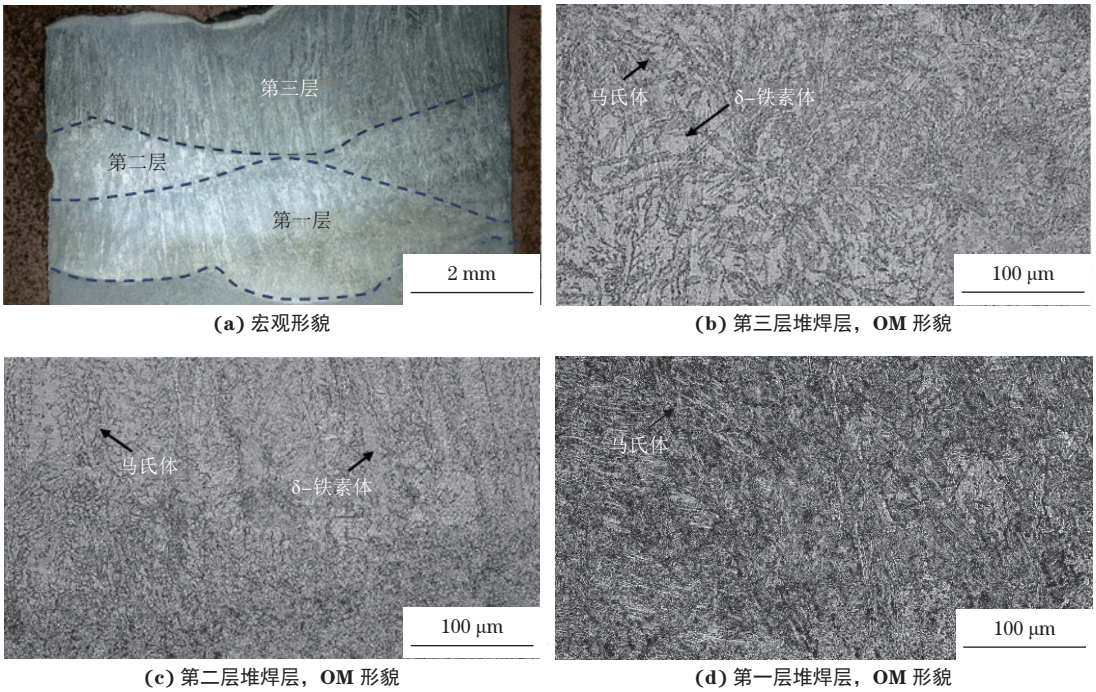

(a) 宏观形貌　(b) 第三层堆焊层，OM 形貌

(c) 第二层堆焊层，OM 形貌　(d) 第一层堆焊层，OM 形貌

图 2　耐磨焊条堆焊层横截面的宏观形貌与 OM 形貌

Fig. 2　Macromorphology (a) and OM morphology (b–d) of cross-section of surfacing layer by cladding with wear-resistant electrode: (b) third layer of surfacing layer; (c) second layer of surfacing layer and (d) first layer of surfacing layer

由图 3 可见：普通焊条堆焊层以针状铁素体和块状铁素体等软相为主，含有少量珠光体。与图 2 对比可知：耐磨焊条堆焊层中的板条马氏体含量更高，尺寸更小，δ-铁素体含量更低且分布更弥散。耐磨焊条堆焊层表现出高马氏体体积分数及细晶特征，这主要归因于药皮中稀土元素的复合作用。稀土在熔池中能起到脱氧、脱硫并净化晶界作用，形成细小稀土氧化物夹杂，从源头抑制粗大扩散型相的形核与长大，促进淬火过程中板条马氏体的形成；这些细小稀土夹杂物在热循环中既能作为异质形核位点，又能对奥氏体晶界运动形成界面阻滞，有效抑制奥氏体长大，最终转变为更细小的马氏体板条[24]。

2.2　硬　度

采用自研耐磨焊条制备的堆焊层中，第三层、第二层和第一层横截面的硬度分别为 340，346，533 HV，普通焊条对应位置的硬度分别为 232，160，165 HV；自研耐磨焊条堆焊层的硬度远高于普通焊条堆焊层，这是因为耐磨焊条堆焊层的晶粒更细小，板条马氏体含量更多，δ-铁素体含量更低且分布更弥散。从堆焊层顶端到母材方向，耐磨焊条堆焊层的硬度升高，这与板条马氏体含量逐层增加，平均尺寸减小有关。

2.3　耐磨性能

由图 4 可见，在摩擦磨损过程中，自研耐磨焊条堆焊层和普通焊条堆焊层均经历急剧摩擦阶段和稳定摩擦阶段。在摩擦起始阶段，摩擦作用破坏了堆焊层表面的氧化膜，导致摩擦阻力急剧增大，摩擦因数急剧上升；随后随着磨屑被压实，摩擦副表面逐渐磨合，摩擦因数先缓慢下降后趋于稳定。耐磨焊条堆焊层稳定后的平均摩擦因数约为 0.75，低于普通焊条(0.93)，说明耐磨焊条堆焊层的滑动运动阻力更小，表面损伤程度更轻[25]。

由图 5 可见：耐磨焊条堆焊层摩擦磨损后表面出现浅而平缓的沟槽，相比之下，普通焊条堆焊层的磨痕更深更宽，沟底高低起伏大、等高线密集。计算

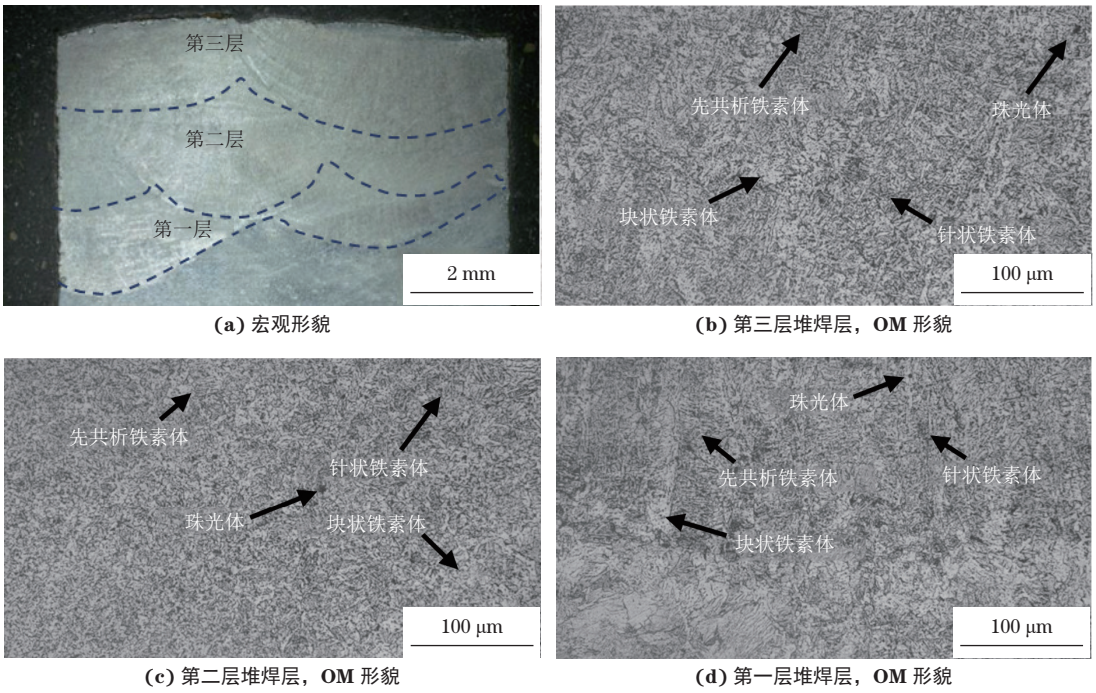

(a) 宏观形貌　(b) 第三层堆焊层，OM 形貌

(c) 第二层堆焊层，OM 形貌　(d) 第一层堆焊层，OM 形貌

图 3　普通焊条堆焊层横截面的宏观形貌与 OM 形貌

Fig. 3　Macromorphology (a) and OM morphology (b–d) of cross-section of surfacing layer by cladding with common electrode: (b) third layer of surfacing layer; (c) second layer of surfacing layer and (d) first layer of surfacing layer

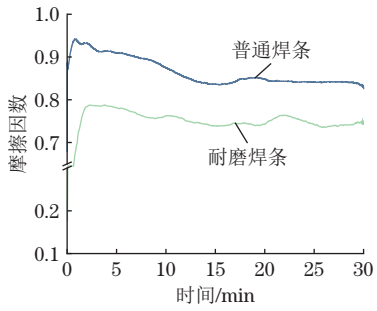

图 4　不同焊条堆焊层的摩擦因数曲线

Fig. 4　Friction coefficient curves of surfacing layers by cladding with different electrodes

得到，耐磨焊条堆焊层和普通焊条堆焊层的磨损率分别为 19.28，66.74 μm² • s⁻¹ • N⁻¹，耐磨焊条堆焊层的磨损率相比普通焊条降低了约 70%。耐磨焊条堆焊层组织中存在的马氏体具有较高的强度和硬度，同时稀土的添加细化了晶粒，减少了缺陷，因此堆焊层耐磨性能较好；普通焊条堆焊层中软相铁素体占比较高，整体强度和硬度较低，在磨损过程中磨粒易嵌入基体，引发塑性变形并对基体产生犁削作用，因此耐磨性能较差[26]。

由图 6 可见，耐磨焊条堆焊层的磨损表面可见浅且粗细均匀的犁沟，伴有部分剥落、少量磨屑及微裂纹，磨损轨迹边缘存在轻微塑性变形，主要磨损机制为轻度磨粒磨损，并伴随黏着磨损。普通焊条堆焊层的磨损表面存在较深犁沟，伴随大量磨屑堆积、剥落、裂纹及明显塑性变形，塑性疲劳磨损剥落痕迹显著[27-28]，磨损机制以黏着磨损为主，并伴随磨粒磨损。

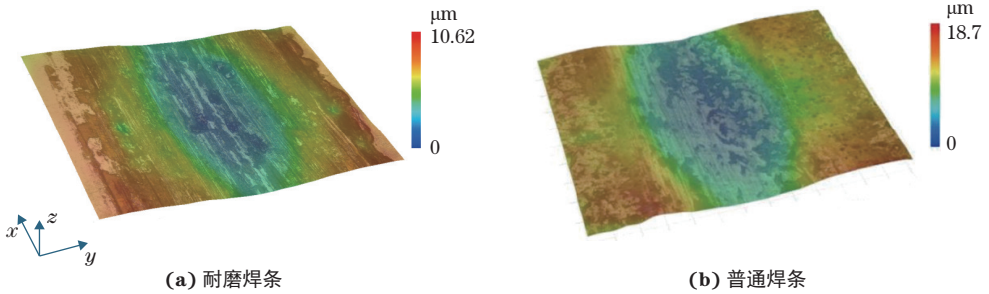

(a) 耐磨焊条　(b) 普通焊条

图 5　不同焊条堆焊层的表面磨损三维形貌

Fig. 5　Three-dimensional wear morphology on surface of surfacing layers by cladding with different electrodes: (a) wear-resistant electrode and (b) common electrode

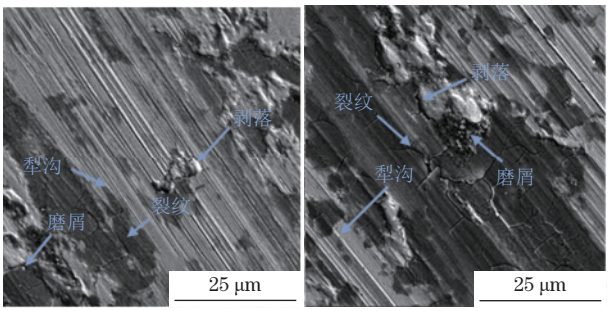

(a) 耐磨焊条　　(b) 普通焊条

图 6　不同焊条堆焊层的表面磨痕形貌

Fig. 6　Wear scar morphology on surface of surfacing layers by cladding with different electrodes: (a) wear-resistant electrode and (b) common electrode

3　结　论

(1)针对水工闸门磨损修复研制的水下耐磨焊条制备的堆焊层中未见明显裂纹缺陷, 组织为板条马氏体和少量 δ-铁素体, 马氏体沿最大温度梯度方向生长形成柱状晶。与普通焊条相比, 耐磨焊条堆焊层的晶粒更细小, 马氏体体积分数更高, δ-铁素体含量更少。

(2)与普通焊条相比, 耐磨焊条堆焊层的显微硬度更高, 磨损率降低了约 70%, 摩擦因数更低, 耐磨性能更好。

(3)耐磨焊条堆焊层的磨损表面存在浅且粗细均匀的犁沟, 局部伴有少量剥落、磨屑及微裂纹, 主要磨损机制为轻度磨粒磨损; 普通焊条堆焊层磨损表面存在较深犁沟和大量磨屑堆积、剥落等特征, 磨损机制以黏着磨损为主。

参考文献:

[1] 张雷, 曹尊毅, 王金亮, 等. 运行工况对多沙河流水轮机导叶区磨损影响研究 [J]. 水利水电技术(中英文), 2022, 53(4): 148-156.
ZHANG L, CAO Z Y, WANG J L, et al. Study on influence of operating conditions on turbine vane wear in sandy river[J]. Water Resources and Hydropower Engineering, 2022, 53(4): 148-156.

[2] KOIRALA R, THAPA B, NEOPANE H P, et al. Sediment erosion in guide vanes of Francis turbine: A case study of Kaligandaki Hydropower Plant, Nepal[J]. Wear, 2016, 362: 53-60.

[3] 郑凯, 蒋致乐, 刘明礼, 等. 流域梯级水电站负荷短期联合优化调度研究 [J]. 电力科技与环保, 2023, 39(4): 305-313.
ZHENG K, JIANG Z L, LIU M L, et al. Study on short-term joint optimal operation of cascaded hydropower stations[J]. Electric Power Technology and Environmental Protection, 2023, 39(4): 305-313.

[4] THAPA B S, THAPA B, DAHLHAUG O G. Empirical modelling of sediment erosion in Francis turbines[J]. Energy, 2012, 41(1): 386-391.

[5] SUN J Q, YANG Y, WANG K, et al. A comparative study on the performance and microstructure of 304NG stainless steel in underwater and air laser welding[J]. Materials, 2024, 17(15): 3854.

[6] 刘新臣. 中小水电站的检修策略及可靠性管理研究 [J]. 电力科技与环保, 2019, 35(4): 49-52.
LIU X C. Maintenance strategy and reliability management for small and medium-sized hydropower stations[J]. Electric Power Technology and Environmental Protection, 2019, 35(4): 49-52.

[7] VACCARI L, SCHEITHAUER T, LENDIEL I, et al. Corrosion behavior of austenitic stainless steel and nickel-based welded joints in underwater wet welding[J]. NPJ Materials Degradation, 2024, 8: 51.

[8] PAN J J, YANG L J, HU S S, et al. Numerical analysis of thermal cycle characteristics and prediction of microstructure in multi-pass UWW[J]. The International Journal of Advanced Manufacturing Technology, 2016, 84(5): 1095-1102.

[9] YOUNES R, TOMKÓW J, IDIR A, et al. Mechanical and structural behavior of high-strength low-alloy steel pad welded by underwater wet welding conditions[J]. The International Journal of Advanced Manufacturing Technology, 2023, 129(11): 5615-5624.

[10] MAGUDEESWARAN G, BALASUBRAMANIAN V, MADHUSUDHAN REDDY G. Effect of welding consumables on hydrogen induced cracking of armour grade quenched and tempered steel welds[J]. Ironmaking & Steelmaking, 2008, 35(7): 549-560.

[11] MENEZES P H R, PESSOA E C P, BRACARENSE A Q. Comparison of underwater wet welding performed with silicate and polymer agglomerated electrodes[J]. Journal of Materials Processing Technology, 2019, 266: 63-72.

[12] SANTOS V R, BRACARENSE A Q, PESSOA E C P, et al. Development of oxyrutile low alloy ferritic electrode for wet welding[J]. Journal of Materials Research and Technology, 2022, 21: 1223-1247.

[13] GUO N, LIU D, GUO W, et al. Effect of Ni on microstructure and mechanical properties of underwater wet welding joint[J]. Materials & Design, 2015, 77: 25-31.

[14] PURNAMA D, WINARTO W, SUSILO F H. Mechanical properties of underwater wet welded marine steel plates

using different low hydrogen electrodes[C]//Proceedings of the 4th International Conference on Engineering, Technology, and Industrial Application (ICETIA) 2017. Surakarta: [s. n.], 2018.

[15] GAO W B, WANG D P, CHENG F J, et al. Microstructural and mechanical performance of underwater wet welded S355 steel[J]. Journal of Materials Processing Technology, 2016, 238: 333-340.

[16] LI H L, LIU D, YAN Y T, et al. Effects of heat input on arc stability and weld quality in underwater wet flux-cored arc welding of E40 steel[J]. Journal of Manufacturing Processes, 2018, 31: 833-843.

[17] WANG J F, MA J K, LIU Y B, et al. Influence of heat input on microstructure and corrosion resistance of underwater wet-welded E40 steel joints[J]. Journal of Materials Engineering and Performance, 2020, 29(11): 6987-6996.

[18] SUROJO E, GUMILANG A H, TRIYONO T, et al. Effect of water flow on underwater wet welded A36 steel[J]. Metals, 2021, 11(5): 682.

[19] 马壮, 张焱鑫, 付栓栓, 等. 硅酸盐矿物在焊条药皮中的应用[J]. 硅酸盐通报, 2014, 33(8): 1984-1988.
MA Z, ZHANG Y X, FU S S, et al. Application of silicate mineral in electrode covering[J]. Bulletin of the Chinese Ceramic Society, 2014, 33(8): 1984-1988.

[20] 李春剑, 徐锴, 冯伟, 等. 稀土在低合金高强钢焊缝金属中的应用与研究现状[J]. 电焊机, 2025, 55(3): 15-27.
LI C J, XU K, FENG W, et al. Research status of rare earth elements in high-strength low-alloy weld metals[J]. Electric Welding Machine, 2025, 55(3): 15-27.

[21] WU Y F, YANG K, CHENG X M, et al. Microstructure and corrosive-wear resistance of surfacing layers for underwater wet welding[J]. Materials Today Communications, 2024, 39: 108675.

[22] CHU R S, FAN Y, LI Z J, et al. Study on the control of rare earth metals and their behaviors in the industrial practical production of Q420q structural bridge steel plate[J]. Metals, 2018, 8(4): 240.

[23] DAS D, CHATTOPADHYAY P P. Influence of martensite morphology on the work-hardening behavior of high strength ferrite-martensite dual-phase steel[J]. Journal of Materials Science, 2009, 44(11): 2957-2965.

[24] 周继烈, 孙中浩, 戴刚平, 等. Ce 对 Q420 钢焊缝力学性能影响的研究[J]. 稀土, 2016, 37(2): 101-106.
ZHOU J L, SUN Z H, DAI G P, et al. Effect of rare earth on weld mechanical properties of Q420 steel[J]. Chinese Rare Earths, 2016, 37(2): 101-106.

[25] CHAUDHARY B, JAIN N K, MURUGESAN J, et al. Friction stir powder additive manufacturing of Al 6061 alloy: Enhancing microstructure and mechanical properties by reducing thermal gradient[J]. Journal of Materials Research and Technology, 2023, 26: 1168-1184.

[26] 彭欢, 胡学文, 王海波, 等. 马氏体体积分数对热轧高强钢的力学性能和耐磨性能的影响[J]. 热加工工艺, 2023, 52(1): 58-61.
PENG H, HU X W, WANG H B, et al. Effect of martensite volume fraction on mechanical properties and wear resistance of hot rolled high strength steel[J]. Hot Working Technology, 2023, 52(1): 58-61.

[27] 蒋成成, 宋庆雷, 张平, 等. 等离子熔覆 $FeCoCrNiAl_{0.5}Ti_{0.5}$ 高熵合金涂层的组织及耐磨性能[J]. 机械工程材料, 2024, 48(10): 1-8.
JIANG C C, SONG Q L, ZHANG P, et al. Microstructure and wear resistance of plasma cladding $FeCoCrNiAl_{0.5}Ti_{0.5}$ high entropy alloy coating[J]. Materials for Mechanical Engineering, 2024, 48(10): 1-8.

[28] MOUSTAFA S F, EL-BADRY S A, SANAD A M, et al. Friction and wear of copper-graphite composites made with Cu-coated and uncoated graphite powders[J]. Wear, 2002, 253(7/8): 699-710.

Microstructure and Properties of Surfacing Layer by Cladding with Wear-Resistant Electrode for Hydraulic Gate Additive Repair

ZHU Sisi[1,2], HU Xing[1,2], WU Yifan[3], ZHAO Jianhua[2], YANG Ke[2]

(1. China Yangtze Power Co., Ltd., Wuhan 210023, China; 2. National Engineering Research Center of Water Resources Efficient Utilization and Engineering Safety, Nanjing 211100, China; 3. College of Mechanical and Electrical Engineering, Hohai University, Changzhou 213000, China)

Abstract: A wear-resistant electrode was designed. The flux coating of the electrode was composed of reduced iron powder, sepiolite ore, potassium feldspar, sodium silicate, rutile, fluorite, manganese powder, cellulose, aluminum-silicon alloy, ferrosilicon alloy and rare earth ferrosilicona. The core was made of 0Cr13 stainless steel wire. Three-layer multi-pass underwater surfacing welding tests were conducted on Q235 steel by self-shielded metal arc welding. The microstructure and wear resistance of the surfacing layer deposited with the wear-resistant electrode were investigated in comparison with those of a conventional electrode. The results show that the surfacing layer deposited with the wear-resistant electrode was free from cracks and other defects, and its microstructure consisted of lath martensite and a small amount of δ-ferrite. The martensite grew along the temperature gradient, forming columnar crystals. Compared with the common electrode deposited surfacing layer, the wear-resistant electrode layer exhibited smaller martensite grain size, a higher volume fraction of martensite, and lower content of δ-ferrite. Compared with that with the common electrode deposited surfacing layer, the microhardness of the wear-resistant electrode deposited surfacing layer increased, and the friction coefficient and the wear rate decreased; the wear-resistance was improved. The worn surface of the wear-resistant electrode deposited surfacing layer exhibited shallow and uniformly sized furrows, accompanied by localized minor spalling, wear debris, and microcracks; the dominant wear mechanism was mild abrasive wear.

Key words: underwater welding; microstructure; microhardness; wear resistance

(上接第 80 页)

Effect of Cerium Content on Microstructure and Tensile Properties of 2319 Aluminum Alloy Components Fabricated by Wire Arc Additive Manufacturing

MENG Xiaohao, YU Shengfu, DENG Fangbin, CHEN Ying

(School of Materials Science and Engineering, Huazhong University of Science and Technology, Wuhan 430074, China)

Abstract: Large cylindrical components of 2319 aluminum alloy with different cerium content (mass fractions of 0.07%, 0.23%, and 0.52%) were fabricated by a twin-wire cooperative arc additive manufacturing process, with ER2319 aluminum alloy wire as the primary wire and cerium-containing flux-cored aluminum wire as the auxiliary wire. The effect of cerium content on the microstructure and tensile properties of the components was studied. The results show that the microstructure of the alloys with different cerium content consisted of an α-Al matrix and secondary phases of Al_2Cu, $Al_{11}Ce_3$, and dislocation pile-ups appeared around the $Al_{11}Ce_3$ phase. When the cerium mass fraction increased to 0.23%, the number of Al_2Cu and $Al_{11}Ce_3$ secondary phases increased and their distribution became more uniform, and grains were refined; the yield strength, tensile strength, and elongation after fracture increased. When the cerium mass fraction increased to 0.52%, the total amount of secondary phases was reduced, and the grains were slightly coarsened; the tensile properties of the alloy decreased. The $Al_{11}Ce_3$ phase formed after cerium addition promoted heterogeneous nucleation due to their small average lattice mismatch (less than 12%) with α-Al, resuting in grain refinement. Second-phase precipitation strengthening made the primary contribution to the enhancement of the alloy's strength, and grain boundary strengthening played a secondary role.

Key words: rare earth element; cerium content; wire arc additive manufacturing; 2319 aluminum alloy; microstructure; grain refinement